Science Advances
AAAS

advances.sciencemag.org/cgi/content/full/5/6/eaaw3192/DC1

Supplementary Materials for

Transport of a graphene nanosheet sandwiched inside cell membranes

Pengyu Chen, Hua Yue, Xiaobo Zhai, Zihan Huang, Guang-Hui Ma, Wei Wei*, Li-Tang Yan*

*Corresponding author. Email: ltyan@mail.tsinghua.edu.cn (L.-T.Y.); weiwei@ipe.ac.cn (W.W.)

Published 7 June 2019, *Sci. Adv.* **5**, eaaw3192 (2019)
DOI: 10.1126/sciadv.aaw3192

The PDF file includes:

Other Supplementary Material for this manuscript includes the following:

(available at advances.sciencemag.org/cgi/content/full/5/6/eaaw3192/DC1)

Movie S1 (.mov format). Detailed translocation pathway of GO across the lipid membrane toward the sandwiched GO structure at $\chi_{GT} = 15.73$.
Movie S2 (.mov format). Detailed translocation pathway of the GO model, representing outcomes from standard oxidization processes with the oxidation degree $\rho_O = 0.3$, across the lipid membrane toward the sandwiched GO structure.
Movie S3 (.mov format). Detailed diffusive dynamics of a sandwiched GO exhibiting Brownian motion at $\chi_{GT} = 1.43$.
Movie S4 (.mov format). Detailed diffusive dynamics of a sandwiched GO exhibiting Lévy walk at $\chi_{GT} = 10.01$.
Movie S5 (.mov format). Detailed diffusive dynamics of a sandwiched GO exhibiting directional motion at $\chi_{GT} = 14.3$.

Supplementary Materials

Section S1. Details of simulation methods, models, and data analysis

Simulation models. Computer simulations use the dissipative particle dynamics (DPD) technique which extends the simulation scales of time and space to be appropriate to the study of nanoparticle−membrane systems with explicit water (*29, 34, 48*). The models of lipid, membrane, and graphene are displayed in fig. S6. Each amphiphilic lipid consists of a head group and two tails (*29, 36*). The head group is constructed by three connected hydrophilic beads and each tail includes three connected hydrophobic beads. 625 lipids self-assemble into a tensionless lipid bilayer membrane spanning the simulation box. Each GO is modeled by arranging the hydrophobic beads on a single layer of fcc (face-centered cubic) lattice into a desired geometrical shape and area. Solvent particles are represented by a single bead.

In the present work, the interaction parameter between GO and lipid tail χ_{GT} is varied to reproduce different oxidization degrees or chemical modifications of the GO. For example, increasing χ_{GT} indicates a higher oxidization degree of the GO due to the reduced attraction between GO and lipid tails. Indeed, upon interacting with the lipid bilayer membrane, the GO model leads to the structures and dynamic behaviors similar with that constructed based on the typical structure model representing outcomes from standard oxidization processes (*29, 51, 52*) (see figs. S7, S8, S14, S15, and S19, and Movies S1 and S2). Furthermore, the results based on such a model are readily generalized to other 2D nanomaterials.

The Young's modulus of the GO model has been calibrated according to the experimentally found elasticity of graphene (*27, 49, 50*). Experiments on bulk graphite give about 1 TPa for the in-plane Young's modulus, while the Young's modulus of graphene varies between 0.5

and 1.0 TPa (*55*). In order to have a similar Young's modulus of our GO model, the modulus of the spring and the modulus of the angle bend between beads of the GO are selected as $700\,\mathrm{kcal}\cdot\mathrm{mol}^{-1}\cdot\mathrm{Å}^{-2}$ and $700\,\mathrm{kcal}\cdot\mathrm{mol}^{-1}\cdot\mathrm{rad}^{-2}$ respectively (*49*).

Details of DPD simulations. In a DPD system, a set of interacting beads is considered, whose time evolution is governed by the following Newton's motion equations (*48*)

$$\frac{d\mathbf{r}_i}{dt}=\mathbf{v}_i,\frac{d\mathbf{v}_i}{dt}=\mathbf{f}_i \tag{1}$$

Furthermore the total force $\mathbf{f}_i$ acting on every bead can be expressed by (*50*)

$$\mathbf{f}_i=\sum_{j\neq i}(\mathbf{F}_{ij}^C+\mathbf{F}_{ij}^D+\mathbf{F}_{ij}^R)+\mathbf{F}_i^S+\mathbf{F}_i^A \tag{2}$$

where $\mathbf{F}_{ij}^C,\mathbf{F}_{ij}^D,\mathbf{F}_{ij}^R,\mathbf{F}_i^S,\mathbf{F}_i^A$ are the conservative force, the dissipative force, the random force, the spring force and the angle force respectively. Here $\mathbf{F}_i^S,\mathbf{F}_i^A$ are additional forces, which are introduced to represent the interactions between bonded beads. The conservative force $\mathbf{F}_{ij}^C$, which is derived from a soft interaction potential within the certain cutoff radius r_c, can be given by the following equation

$$\mathbf{F}_{ij}^C=\begin{cases}a_{ij}(1-\dfrac{r_{ij}}{r_c})\mathbf{e}_{ij} & (r_{ij}<r_c)\\ 0 & (r_{ij}\geq r_c)\end{cases} \tag{3}$$

where $\mathbf{r}_{ij} = \mathbf{r}_i - \mathbf{r}_j$, $r_{ij} = |\mathbf{r}_{ij}|$ and $\mathbf{e}_{ij} = \mathbf{r}_{ij} / r_{ij}$. a_{ij} is the maximum repulsion between bead *i* and bead *j*, which is related with the Flory-Huggins χ-parameter (χ_{ij}) as follow

$$\chi_{ij} = \frac{\alpha_{ij} - \alpha_{ii}}{3.27} \tag{4}$$

where a_{ii} is the repulsion parameter between the same type beads and $a_{ii} = 25$ is used in our DPD system. α_{ij} will be smaller than 25 for a strong attraction between two beads while it will be larger than 25 for a strong bead-bead repulsion interaction. Furthermore, the decrease of α_{ij} corresponds to the enhancement of bead attraction and vice versus. For the present simulations, each parameter is selected carefully based on the properties and interactions of different beads (*27, 29, 49*).

The dissipative force $\mathbf{F}_{ij}^D$ and the random force $\mathbf{F}_{ij}^C$ act together as a thermostat and can be given by the following formulas

$$\mathbf{F}_{ij}^D = -1/2\sigma^2\omega^D\left(r_{ij}\right)(\mathbf{v}_{ij} \cdot \mathbf{e}_{ij})\mathbf{e}_{ij} \tag{5}$$

$$\mathbf{F}_{ij}^R = \sigma\omega^R\left(r_{ij}\right)\xi_{ij}\Delta t^{-1/2}\mathbf{e}_{ij} \tag{6}$$

where $\mathbf{v}_{ij} = \mathbf{v}_i - \mathbf{v}_j$ and ξ_{ij} is a random number which has zero mean and unit variance. The noise amplitude σ is fixed at 3 and we take

$$w^D(r_{ij}) = \left[w^R(r_{ij}) \right]^2 = \begin{cases} (1-\frac{r_{ij}}{r_c})^2 & (r_{ij} < r_c) \\ 0 & (r_{ij} \geq r_c) \end{cases} \quad (7)$$

This particular thermostat is special in that is conserved angular momentum, which leads to a correct description of hydrodynamics.

A modified velocity-Verlet algorithm due to Groot and Warren is used to solve the motion equation (*48*). In details, we take the bead mass, the cutoff radius and the temperature as units and define the time scale as $\tau = \sqrt{m r_c^{\,2} / k_B T}$. The size of our simulation box is $20 \times 20 \times 20\, r_c^3$ and periodic boundary condition in all directions is taken into account. To prevent the passage of fluid beads through the GO, an additional bounce-back boundary condition is imposed on the GO surfaces (*56*). In order to assure the accurate temperature control of the simulation system, we set $\Delta t = 0.008\,\tau$ as the time step and select a bead number density of $3/r_c^3$.

The reduced DPD units can be converted to SI units by examining the membrane thickness and the lipid diffusion coefficient. In a tensionless dipalmitoylphosphatidylcholine (DPPC) membrane, the typical area per lipid is about 0.64 nm (*57*). We use this value to estimate the physical length of our simulations and get that r_c is about 0.7 nm. Thereby the area of the planar membrane in our simulation is about 14 nm $\times$ 14 nm. Moreover, we relate the time unit τ to the physical time by comparing the in-plane diffusion coefficient of lipids. A typical experimental result of this diffusion coefficient is $5\,\mu m^2/s$ (*34*). Thus we can get τ =7.7 ns and the total physical time of each calculation is over 0.3 ms (5×10^6 time steps).

Double-Membrane System. To mimic the diffusion of drug beads within a cell, a double bilayer system is built, which divides the system into two regions: an "extracellular" region without drug bead and an "intracellular" region where the drug beads can be added into it (*58*). The model of double bilayer system is displayed in fig. S6. Each receptor, which will be targeted by the drug beads, is modeled as a cluster of frozen DPD beads grouped into a rigid body with fcc-arranged beads (*53*). The diameter of cylindrical receptor is set as $R = 2\ r_c$, and the height is set as $h=2h_1+h_2=2*3+4=10\ r_c$, where h_1 and h_2 represent the height of solvophobic block and solvophilic block, respectively. Two patches of identical lipid membranes have a total of 1952 lipid molecules, with each membrane possessing 976 lipids. The double lipid membrane system is constructed to be an elongated rectangular box along *z* axis to prevent two bilayers from affecting each other. The size of the system is $25\times 25\times 60\ r_c^3$, with periodic boundary condition in all directions. The lower membrane is 10 r_c away from the bottom of the box while the upper membrane is 20 r_c away from the top. Drug beads are represented by a single DPD bead.

Trajectory analysis. The trajectories of persistent segments and jiggling periods are identified using the wavelet analysis method described elsewhere (*38*). Briefly, the wavelet analysis method comprises following three steps:

Firstly, choose an appropriate wavelet. The wavelet is a weighting function which is used in calculating the local integral values of time series over different scales. Wavelets can take different forms and thereby can acquire different integral values. Typically, "Haar wavelet" is commonly used in the wavelet analysis.

Secondly, perform the wavelet transform. The wavelet transform is mathematically defined as a local integral. During the wavelet transform, the time-dependent data can be

transformed into a time- and scale-dependent representation of the original data. In practice, the transformation is easy to conduct using an easily accessible toolbox MATLAB.

Finally, determine the scale and threshold. We must set a scale on which a threshold is used to decide what differences are large enough to matter. This threshold serves as the decision criterion for classifying the type of dynamics and identifying dynamical heterogeneity.

In our simulations, we computed the Haar wavelet coefficients at a scale of 500 frames for all trajectories. At this scale, the wavelet transform coefficients can be clearly distinguished. The threshold was set according to the "universal thresholding"[19]. Combining results both on *x* and *y*, the separation is overlaid on the original trajectory in the inset of Fig. 2B, with persistent segments highlighted in red. Fig. 2D shows that the assigned persistent segments are super-diffusive while jiggling segments exhibit Fickian, which is reasonable physically.

Statistical analysis. After identifying the persistent segments and jiggling periods from the origin trajectory, the angles between the neighboring persistent segments are defined as turning angle (fig. S10), which is statistically uncorrelated and distributed isotropically (Fig. 2F). To calculate the length distribution of persistent segments, we use an equal number of data points per bin (*39*).

To distinguish the exponential and power-law distributions, we use the following method of model selection to provide more evidence[24]. In this method, for a given data set $\mathbf{x}=\{x_1, x_2, x_3, \cdots, x_n\}$ and considering the tail to start at *a*, the power-law tail has probability density function of $f_1(x)=(\mu-1)\mathrm{a}^{\mu-1}x^{-\mu}, x\geq a$, leading to the log-likelihood function

$$\log[L_1(\mu \mid \text{data } \mathbf{x})] = \text{n}\log(\mu - 1) + n(\mu - 1)\log a - \mu\sum_{j=1}^{n}\log x_j \tag{8}$$

The exponential tail has probability density function of $f_2(x) = \lambda e^{-\lambda(x-a)}, x \geq a$, leading to the log-likelihood function

$$\log[L_2(\lambda \mid \text{data } \mathbf{x})] = \text{n}\log\lambda + n\lambda a - \lambda\sum_{j=1}^{n}\log x_j \tag{9}$$

Solving for the maximum likelihood estimates analytically gives $\hat{\mu} = 1 - n/(n\log a - \sum_{j=1}^{n}\log x_j)$ and $\hat{\lambda} = 1/(\sum_{j=1}^{n}\log x_j / n - a)$. Akaike's information criterion for model *i* is

$$\text{AIC}_i = -2\log[L_i(\theta_i \mid \text{data } \mathbf{x})] + 2K_i \tag{10}$$

where $\hat{\theta}_1 = \hat{\mu}, \hat{\theta}_2 = \hat{\lambda}$ and K_i is the number of parameters being estimated for model *i*. The Akaike weights are relative likelihoods of each model, given by

$$w_i = \frac{e^{-\Delta_i/2}}{e^{-\Delta_1/2} + e^{-\Delta_2/2}} \tag{11}$$

where $\Delta_i = \text{AIC}_i - \text{AIC}_{\min}$.

In our simulations, with the data sets containing at least 2000 persistent segments for each χ_{GT}, using Akaike weights can identify the more likely model for the tails, which can eliminate the bias of model selection.

Section S2. Details of analytical models

Detailed deduction of the analytical model of sandwiched-GO-induced pore. We develop an analytical model to understand the simulation results and rationalize the four regimes of the membrane-pore states observed in simulations. Our model is based on the idea of pore formation induced by the repulsive interaction between GO and lipid tails. In the presence of the interaction, the membrane is no longer tensionless. Instead, the sandwiched GO causes an internal membrane tension, which leads to the pore formation.

The energy cost of pore formation in the cell membrane is given by (*59*)

$$E_R = 2\pi R\gamma - \pi R^2\sigma \tag{12}$$

where R is the radius of the circular pore; σ and γ are the membrane tension and the line tension, respectively. In general, γ is a constant for a pure lipid bilayer.

A schematic illustration regarding the GO-induced pore in the membrane is presented in Fig. 4a. Due to the symmetry between the inner and outer leaflets of the cell membrane, we only calculate one single leaflet of the membrane for simplicity. In this system, the interaction energy between GO and lipid tails is $E_a = K_a A_{GT} = K_a(a^2 - \pi R^2)$, where K_a is the area density of interaction energy between GO and lipid tails. With a circular pore of

radius R emerging on the GO of side length a, $A_{GT} = a^2 - \pi R^2$ stands for the contacting area of GO with lipid tails.

Therefore, GO-induced internal membrane tension is calculated as

$$\sigma = E_a / A_m = K_a (a^2 - \pi R^2) / A_m \tag{13}$$

where A_{m} denotes the membrane area.

After substituting Eq. (13) into Eq. (12), the energy of pore formation reads

$$\begin{aligned} E_R &= 2\pi R\gamma - \pi R^2 \sigma \\ &= 2\pi R\gamma - \pi R^2 [K_a (a^2 - \pi R^2) / A_m] \\ &= 2\pi\gamma R - K_a \frac{\pi a^2}{A_m} R^2 + K_a \frac{\pi^2}{A_m} R^4 \end{aligned} \tag{14}$$

The equilibrium radius of pore R_0 is determined by minimization of the pore energy E_R with respect to R

$$\partial_R E(R) = 2\pi\gamma - 2K_a \frac{\pi a^2}{A_m} R + 4K_a \frac{\pi^2}{A_m} R^3 = 0 \tag{15}$$

which admits the following solutions when $K_a \geq K_{a0} = \frac{\gamma A_{\mathrm{m}}}{a^3} \sqrt{\frac{27}{2}\pi}$

$$\begin{cases} R_{01} = 2a\sqrt{\dfrac{1}{6\pi}}\cos\dfrac{\theta}{3} \\ R_{02} = 2a\sqrt{\dfrac{1}{6\pi}}\cos(\dfrac{\theta}{3}-\dfrac{2}{3}\pi) \end{cases} \tag{16}$$

where $\theta = \arccos(-\dfrac{\gamma A_{\mathrm{m}}}{K_a a^3}\sqrt{\dfrac{27}{2}\pi})$ (another solution will no longer be considered because $R_{03} = 2a\sqrt{\dfrac{1}{6\pi}}\cos(\dfrac{\theta}{3}+\dfrac{2}{3}\pi) < 0$).

To determine the energy-minimum solution, we move on to calculate the second-order derivative of pore energy

$$\partial_R^2 E_R = \frac{2\pi K_a}{A_m}(6\pi R^2 - a^2) \tag{17}$$

Substituting R_{01} and R_{02} into Eq. (10), we find that $\partial_R^2 E_R(R_{01}) \geq 0$ and $\partial_R^2 E_R(R_{02}) \leq 0$. Thus, $R_{01} = 2a\sqrt{\dfrac{1}{6\pi}}\cos\dfrac{\theta}{3}$ corresponds to the minimum of pore energy, while $R_{02} = 2a\sqrt{\dfrac{1}{6\pi}}\cos(\dfrac{\theta}{3}-\dfrac{2}{3}\pi)$ gives the maximum of pore energy. A straightforward calculation of R_{01} leads to $\dfrac{\pi R_{01}^2}{a^2} = \dfrac{2}{3}\cos^2\dfrac{\theta}{3}$. Note that θ is a variable depending on K_{a}. Therefore, we obtain the relationship between the ratio of the pore area with the GO area and K_{a} (red curve in Fig. 4D), which fits the simulation results quantitatively.

Furthermore, at the transition point of $K_a = K_{a0}$, one finds that Eq. (15) admits repeated roots of $R_{01} = R_{02} = a/\sqrt{6\pi}$, which means that

$$\begin{cases} \partial_R E_R \mid_{R=R_{01}=R_{02}} = 0 \\ \partial_R^2 E_R \mid_{R=R_{01}=R_{02}} = 0 \end{cases} \tag{18}$$

With increasing K_a to $K_a > K_{a0}$, the two roots depart from each other and R_{01}, R_{02} represent the minimum and the maximum point, respectively, as analyzed before. In fig. S16, we plot E_R-R at different $K_a \geq K_{a0}$. It is found that, when $K_a > K_{a0}$, with the increase of K_a, R_{01} increases, while R_{02} decreases. Moreover, in this figure the curves of R_{01} and R_{02} are presented with respect to various K_a.

Rationalizing the four regimes of membrane-pore states. Now, we rationalize the four regimes illustrated in Fig. 5A based on the analytical model.

Firstly, the boundary between state I (without pore) and state II (unstable state) is acquired by the simulation results (Fig. 3F). Specifically, in state I, no pore is observed in the simulation, while, in state II, pores begin to emerge. The difference between these two regimes represents the dependence of pore energy on the value of K_a, which is characterized by the first-order derivative

$$\frac{\partial E_R}{\partial K_a} = -\pi R^2 \frac{\partial \sigma}{\partial K_a} = -\frac{\pi R^2}{A_m}(a^2 - \pi R^2) \tag{19}$$

Here, $a^2 - \pi R^2 > 0$, leading to $\frac{\partial E_R}{\partial K_a} < 0$. Thus, for a given R, with the increase of K_a, the energy of the pore E_R decreases. In other words, at the larger value of K_a, the pore is easier to be formed in the membrane under the disturbance of thermal energy.

Secondly, we determine the boundary between state II and state III (metastable state) as $K_a = K_{a0}$. Specifically, the transition point $K_{a0} = \frac{\gamma A_m}{a^3}\sqrt{\frac{27}{2}\pi}$ is determined by requiring $|\cos\theta| = |-\frac{\gamma A_m}{a^3 K_a}\sqrt{\frac{27}{2}\pi}| \le 1$. At $K_a = K_{a0}$, there are repeated roots for Eq. (15), *i.e.*, $R_{01} = R_{02} = a/\sqrt{6\pi}$. When $K_a < K_{a0}$, Eq. (15) has no real roots, namely, no minimum value of the pore energy exists, whereas the real roots of Eq. (15) emerge at $K_a \ge K_{a0}$. This transition point defines the boundary to divide state II and state III in Fig. 5A.

Finally, to determine the boundary between state III and state IV (stable state), we define the energy barrier in the E_R-R curve, $\Delta E = E(R_{02}) - E(R_{01})$, as illustrated in Fig. 4B. In a real system, there always exists thermal fluctuations of characteristic energy 1 $k_B T$, which can lead the pore to spontaneously disappear if the energy barrier $\Delta E < 1\ k_B T$. Fig. 5B shows the plot of ΔE versus K_a. It is found that ΔE is a monotonic increasing function. Namely we can find an intersection point at $\Delta E(K_{a1}) = 1\ k_B T$. When $K_a > K_{a1}$, $\Delta E > 1\ k_B T$ is always satisfied. Here, K_{a1} is the boundary to divide state III and state IV.

In conclusion, we give the rational boundaries between the four regimes. For the boundary between state I and state II, it is determined by the simulation results, whereas we can prove that the pore is easier to be formed at larger values of K_a according to the analytical model. The boundary between state II and state III is given by $K_a = K_{a0}$, which is obtained from mathematical analysis. However, due to the presence of thermal fluctuations, the pore can spontaneously disappear in both state II and state III. Therefore, physically, the state II and state III are equivalent. The boundary between state III and state IV is determined by the

occurrence of an energy barrier of ΔE=1 $k_B T$. These three states (state II and state III behave as one state) can be overlapped well with the three diffusive dynamics, thereby explaining the mechanisms of Lévy walk and directional motion of the sandwiched GO.

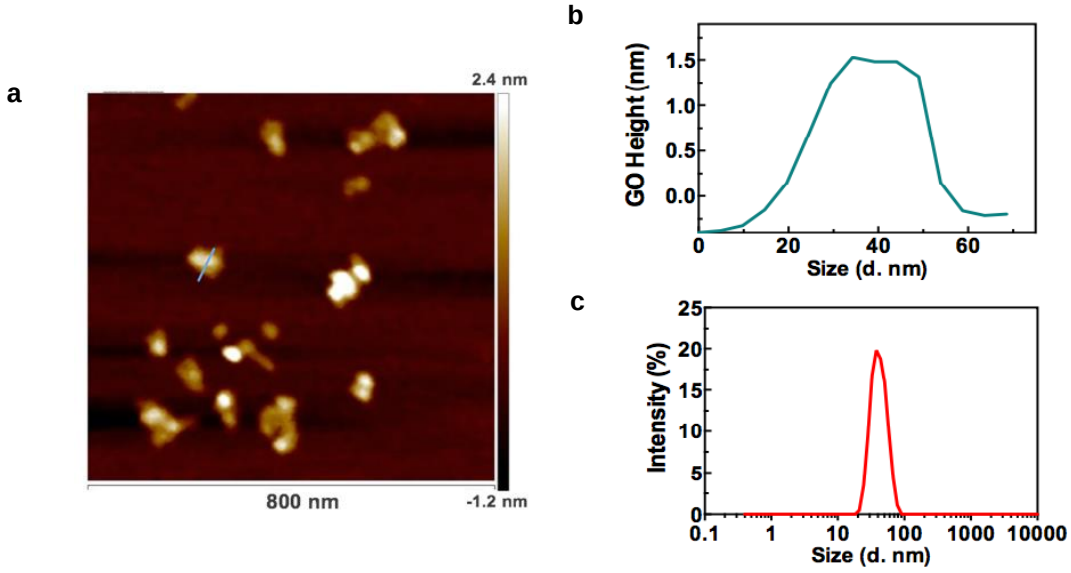

Fig. S1. Characterizations of the prepared 2D material of GO. The AFM image (a), height analysis (b), and size distribution data (c) of a GO showing that the lateral dimension of GO is ~40 nm, and the average height is less than 2 nm (1-2 layers).

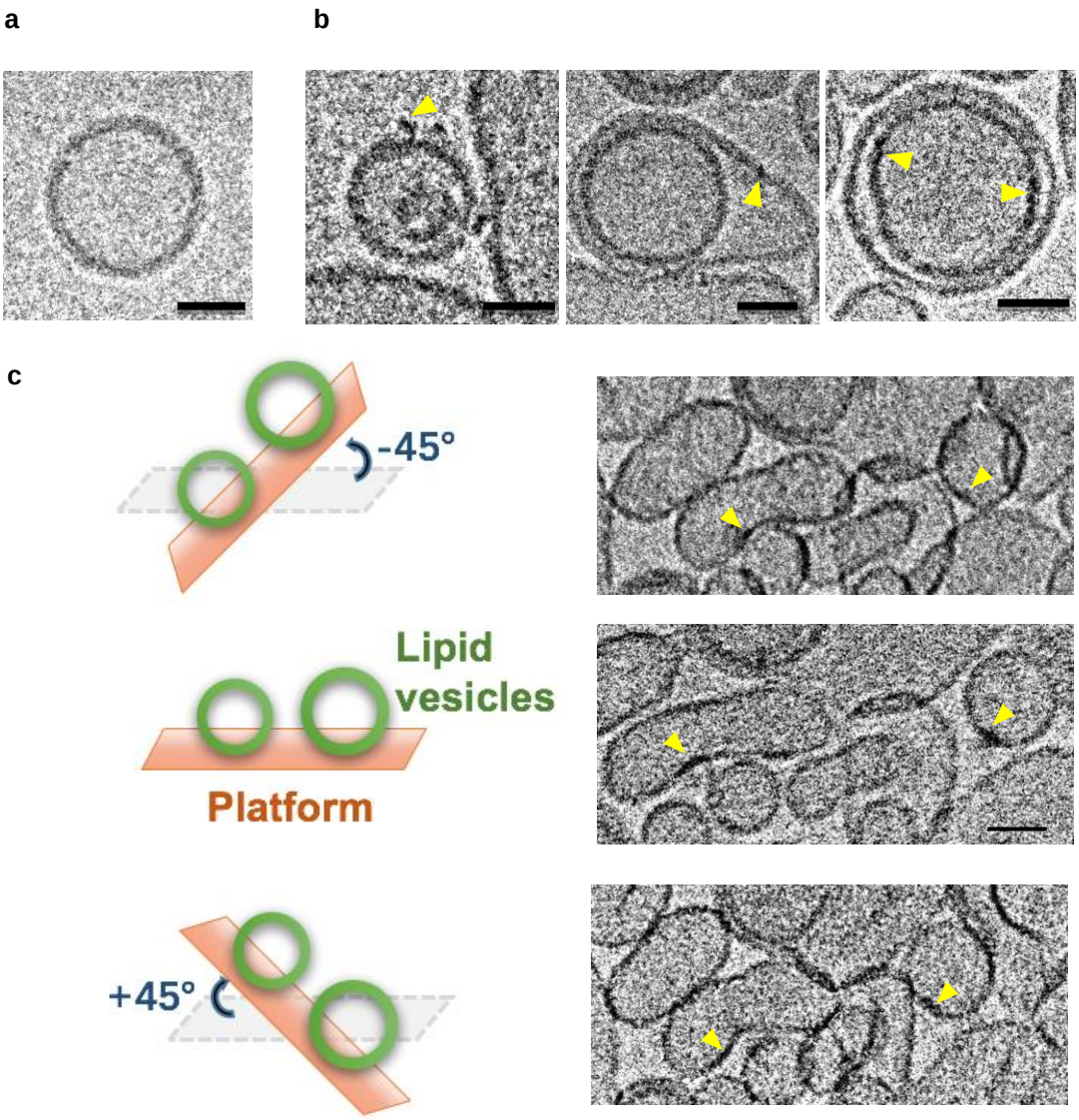

Fig. S2. Cryo-TEM images of the blank liposomes, the formation process of the sandwiched GO superstructure, and the sandwiched structure at different detection angles. Cryogenic transmission electron microscopy (Cryo-TEM) images of the blank liposomes (a), the formation process of sandwiched GO superstructure (b) and the sandwiched structure at different detection angles (c). GO are indicated by the triangles. The darker line (with higher mass density) at 0° is still existing after a total 90° alteration of the detection angle, which reconfirm the sandwiched structure of GO in lipid membrane. Scale bars, 50 nm.

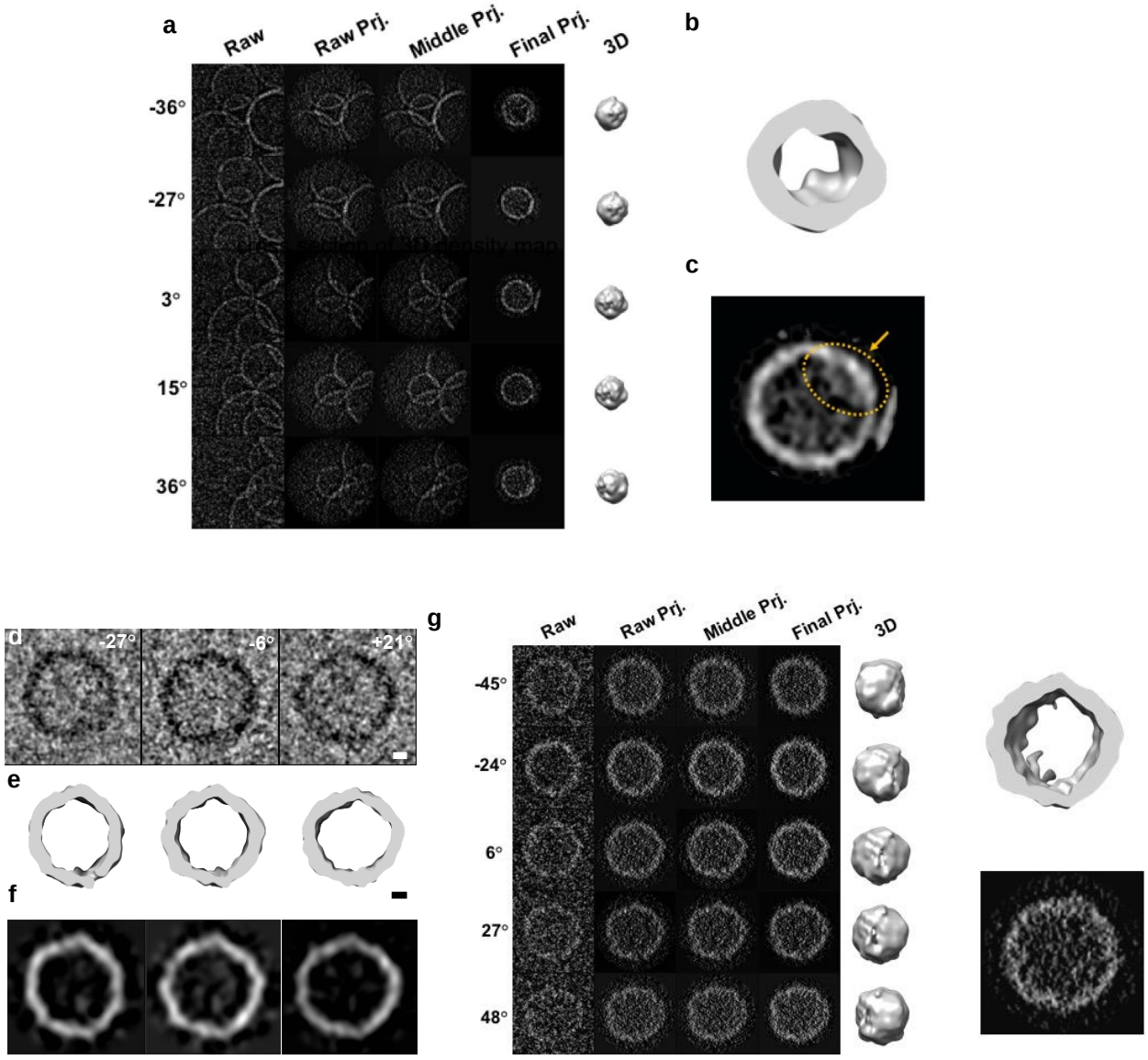

Fig. S3. Tomography views of the 3D map for the GO-membrane superstructure and the blank liposome vesicles. Tomography views of 3D map for the GO-membrane superstructure (a-c) and the blank liposome vesicles (d-g). **a**, Construction process of the 3D map for GO-membrane. **b**, Cross section of 3D density map for GO-membrane. **c**, The projection of 3D map in 0° tilt angle for GO-membrane. The lipid vesicle in the presence of GO nanosheet shows higher mass density as indicated by the looped zone and the arrow. **d**, Raw data. **e**, 3D slice of density map. Scale bar 20 nm. **f**, The middle layers of 3D slices of density map. The density is relatively homogenous for the blank lipid vesicles. **g**, Construction process of 3D map.

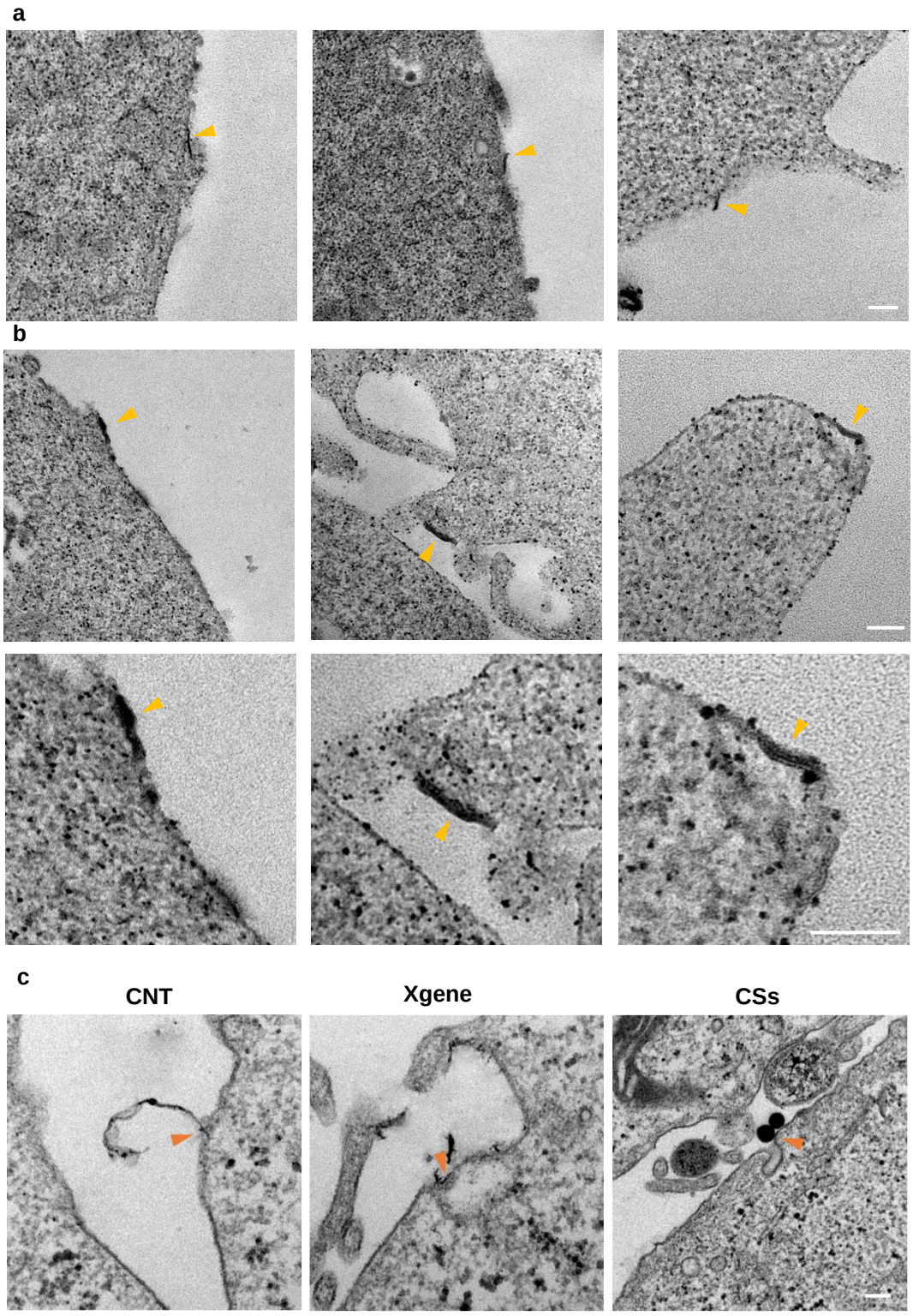

Fig. S4. A series of TEM images of the GO–cell membrane interaction and the cells after exposure to different dimensional materials. The GO-cell membrane interaction includes (a) primary contact and (b) sandwiched status in the membrane (top) and their zoomed image (bottom). Scale bars, 50 nm. **c**, Different dimensional materials include 1D

carbon nanotube (CNT), 2D graphene analogue (Xgene), and 3D carbon spheres (CSs). The Xgene is observed to be hosted inside the cell membrane, similar with that for GO. While the CNT and CSs are found to intimately contact with the cell membrane, no sandwiched superstructure is found for these two materials. Scale bar, 100 nm.

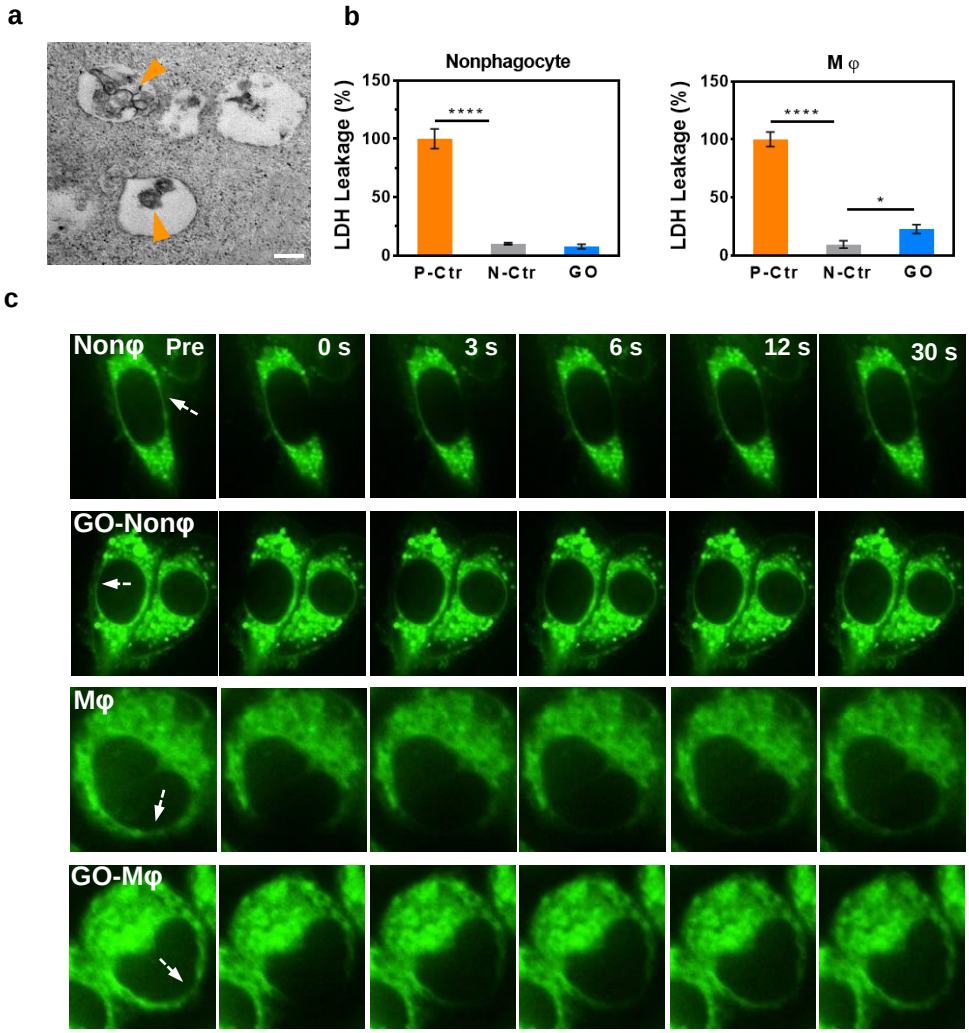

Fig. S5. The interaction between GO and the cells. a, TEM images showing that the GOs are sequestered in the phagosomes after internalization through the macrophage. Scale bar, 50 nm. **b**, LDH leakage data of the GO-treated nonphagocyte and macrophage. No LDH leakage was detected for the GO-treated nonphagocyte (left), while a little LDH leakage was tested for macrophage (right). This phenomenon is in line with the entry capacity of GO for different cell lines. **c**, FRAP images of corresponding cell-GO interactions. The fluidity of membrane lipids was found to be accelerated after GO introduction..

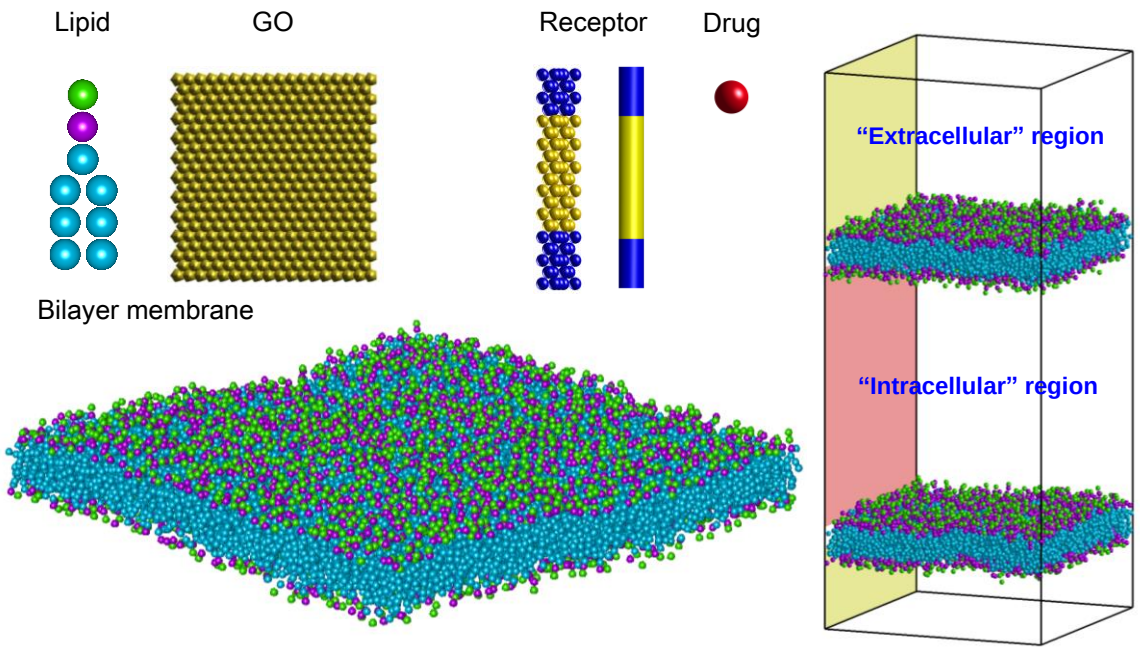

Fig. S6. Molecular models for the individual entities used in the simulations. The model of amphiphilic lipid consists of a head group with three hydrophilic beads and two tails including three hydrophobic beads. In this lipid model, the colors of the beads stand for: head bead with charge +1 (green), head bead with charge -1 (pink), head bead without charge and tail bead (cyan). Each graphene oxide (GO) is modeled by arranging the beads on a single layer of fcc (face-centered cubic) lattice into a desired area (yellow). Lipids self-assemble into a lipid bilayer membrane spanning the simulation box. Each receptor is modeled as a cluster of frozen DPD beads grouped into a cylindrical rigid body with fcc-arranged beads. The solvophobic block and solvophilic block of the transmembrane receptor are represented by yellow and blue, respectively. Drug beads are represented by a single DPD bead (red). The double lipid membrane system is constructed to be an elongated rectangular box along *z* axis, which divides the system into two regions: an "extracellular" region without drug bead and an "intracellular" region where the drug beads can be added into it. For clarity, water beads are not shown.

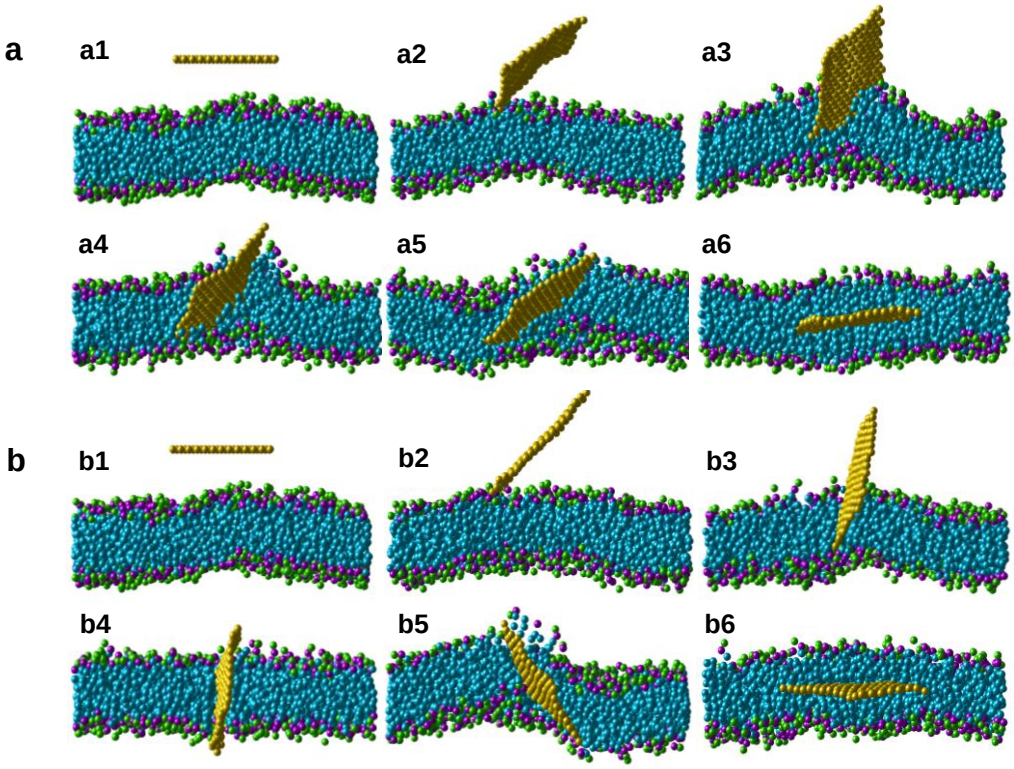

Fig. S7. Translocation pathways of GO across the lipid membrane toward the sandwiched GO structure. a and **b**, Successive stages of a translocation pathways where the interaction parameter between GO and lipid tail, χ_{GT} is: **a**, 1.43; and **b**, 15.73. The times of the slices are: **a1**, 0τ; **a2**, 624τ; **a3**, 640τ; **a4**, 656τ; **a5**, 688τ; and **a6**, 720τ; **b1**, 0τ; **b2**, 620τ; **b3**, 640τ; **b4**, 664τ; **b5**, 800τ; and **b6**, 880τ. Only the *x*-*z* cross section view of the lipid membrane around the GO is shown in each snapshot for clarity.

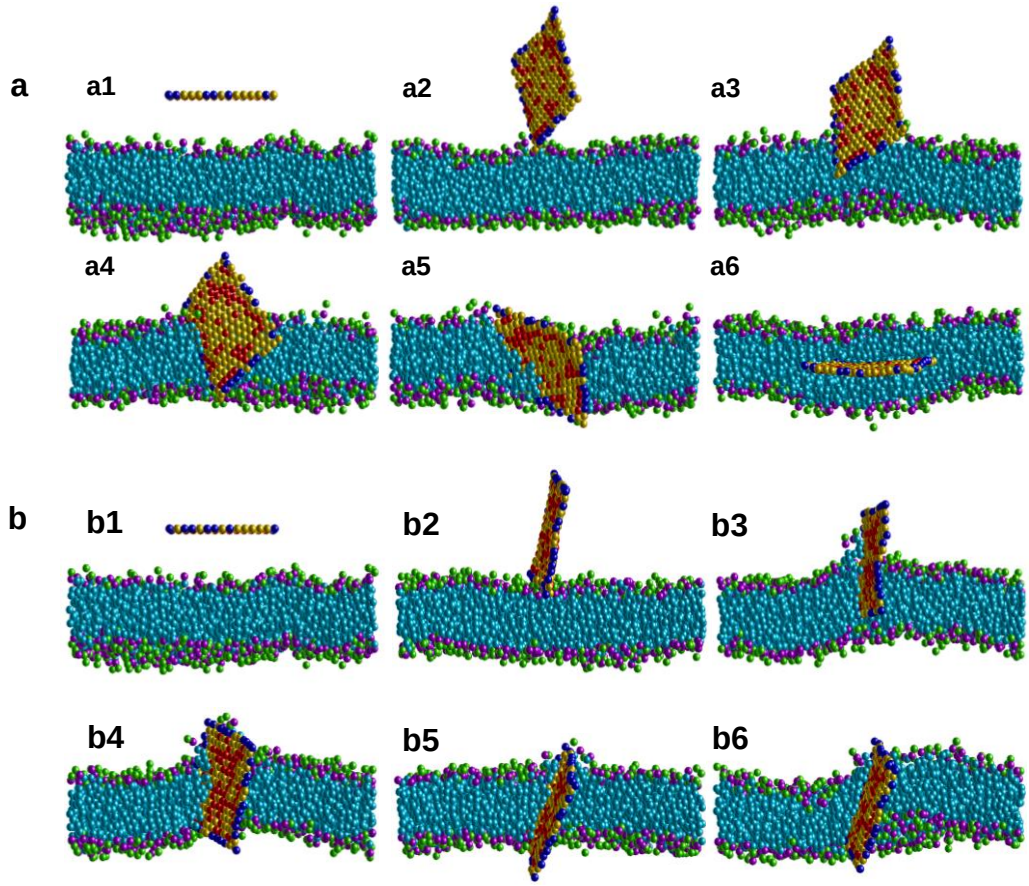

Fig. S8. Translocation pathways of GO, with the model representing outcomes from standard oxidization, across the lipid membrane. a, Successive stages showing the detailed translocation pathway of the GO with the oxidation degree ρ_O=0.3 towards the sandwiched-GO structure. The times of the simulation snapshots are: **a1**, 0τ; **a2**, 100τ; **a3**, 120τ; **a4**, 144τ; **a5**, 1012τ; and **a6**, 1264τ. **b**, Successive stages showing the detailed translocation pathway of the GO with the oxidation degree ρ_O=0.4 towards the structure lying across the membrane. The times of the simulation snapshots are: **b1**, 0τ; **b2**, 1240τ; **b3**, 1320τ; **b4**, 1480τ; **b5**, 1600τ; and **b6**, 2400τ. The colors of yellow, blue, and red indicate the beads of the unoxidized basal plane, the oxidized edge, and the oxidized basal plane. Only the *x*-*z* cross section view of the lipid membrane around the GO is shown in each snapshot for clarity.

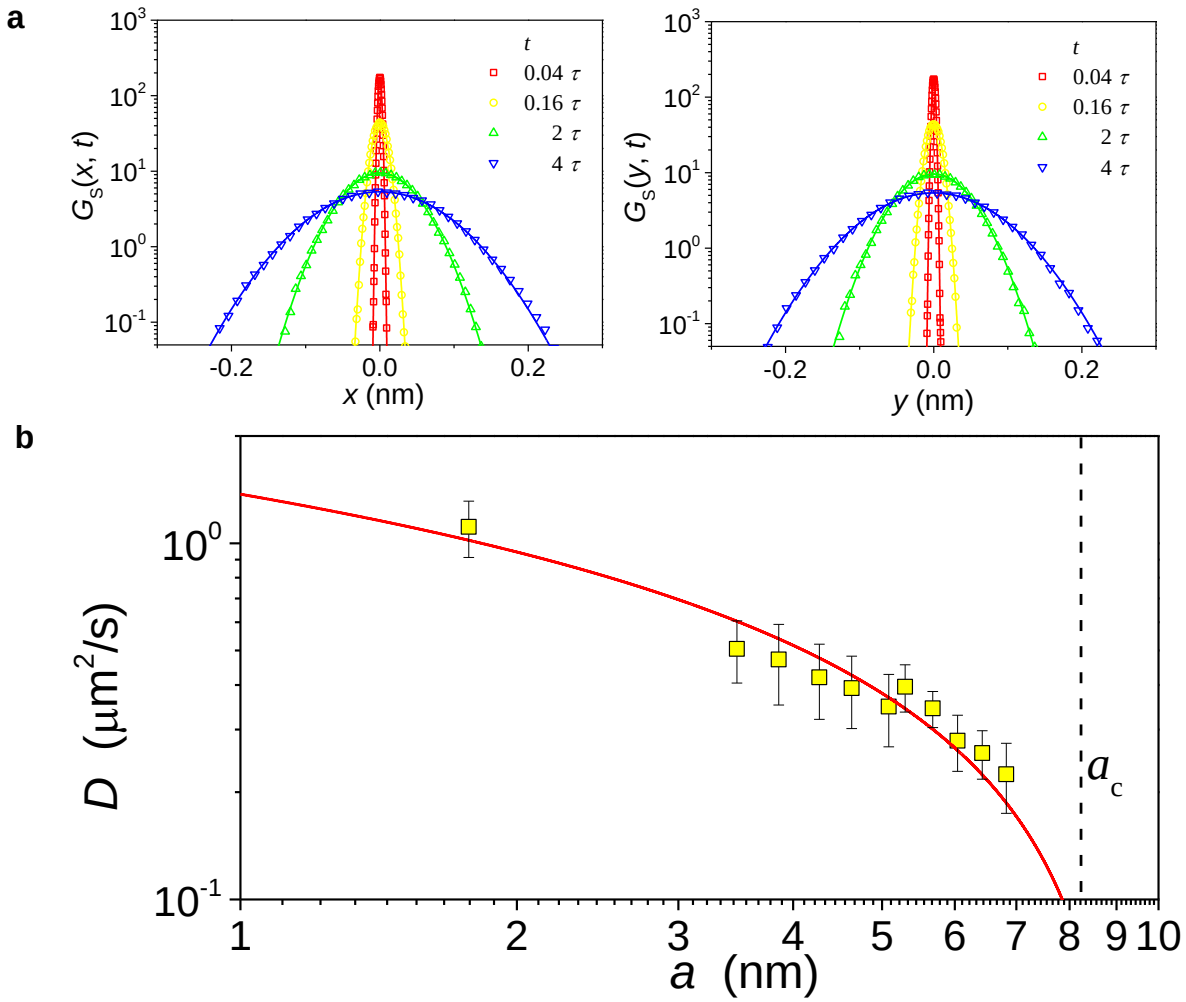

Fig. S9. The displacement probability distributions and the translational diffusion coefficients of the GO sandwiched inside the membrane. a, The displacement probability distributions exhibit Gaussian for several representative values of time step. Averaged from 5 million time steps, the displacement probability distributions of GO sandwiched in lipid bilayer are plotted logarithmically against linear displacement at χ_{GT} =1.43 along *x*-axis (left) and *y*-axis (right). **b**, The translational diffusion coefficients of the GO sandwiched inside membrane can be well described by the SD model. Lateral diffusion coefficient *D* of the GO is plotted as a function of side length, *a*. The solid red line shows the data fit using the SD model. Vertical dashed line denotes the critical size a_c for the SD fitting. This fit gives an estimate of the membrane surface viscosity $\eta_m \approx 0.1778\,\mathrm{Pa\cdot s}$, as well as the

viscosity of the surrounding water $\eta_c \approx 0.03243\,\mathrm{Pa\cdot s}$. The critical radius can be thereby determined as $a_c = h\eta_m / (2\eta_c) \approx 8.2239\,\mathrm{nm}$.

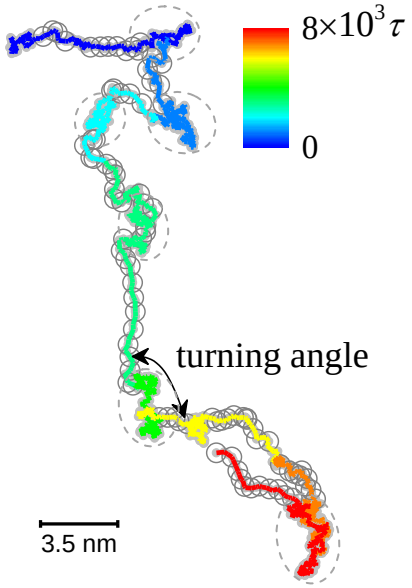

Fig. S10. A schematic diagram illustrating the definition of the turning angle between the neighboring persistent segments. A representative trajectory of GO exhibiting Lévy dynamics is presented in this figure. The color of the line denotes elapsed time with scale shown in the inset, and the persistent segments identified by wavelet analysis are highlighted by circles. The dashed circles mark jiggling periods.

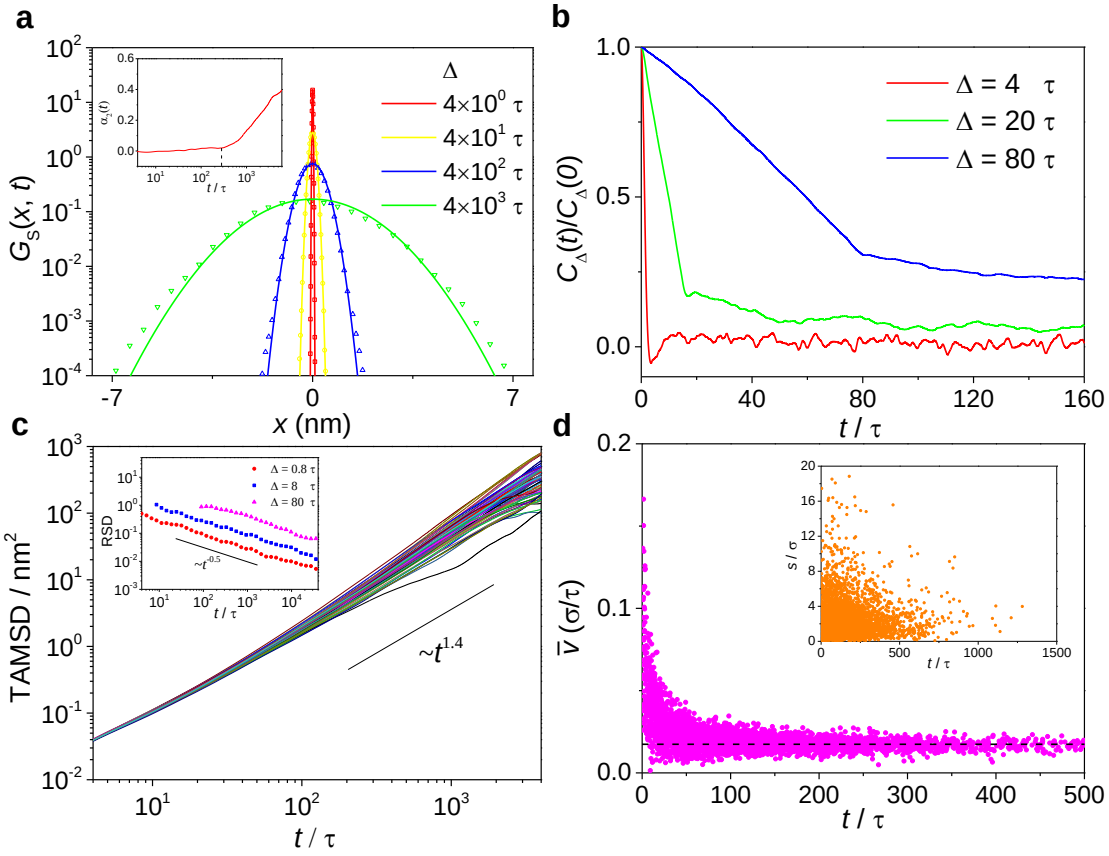

Fig. S11. Diffusive properties of GO with χ_{GT} = 7.15. a, Displacement probability distributions of GO sandwiched in lipid bilayer are plotted logarithmically against linear displacement along *x*-axis. The solid lines represent the Gaussian distribution. Inset: 2D non-Gaussian parameter $\alpha_2(t)$ with dramatic departure from 0 at large time. **b**, Normalized displacement autocorrelation function (DAF) $C_\Delta(t)/C_\Delta(0)$ of the GO for different lag times (*8*). **c**, MSDs of 62 trajectories of the GO. The measurement time for each trajectory is 40000. Inset: Relative standard deviation (RSD) of time-averaged MSDs of the GO for different lag times (*8*). **d**, Averaged speeds of persistent segments as a function of flight time. Inset: The plot of persistent length with jiggling time.

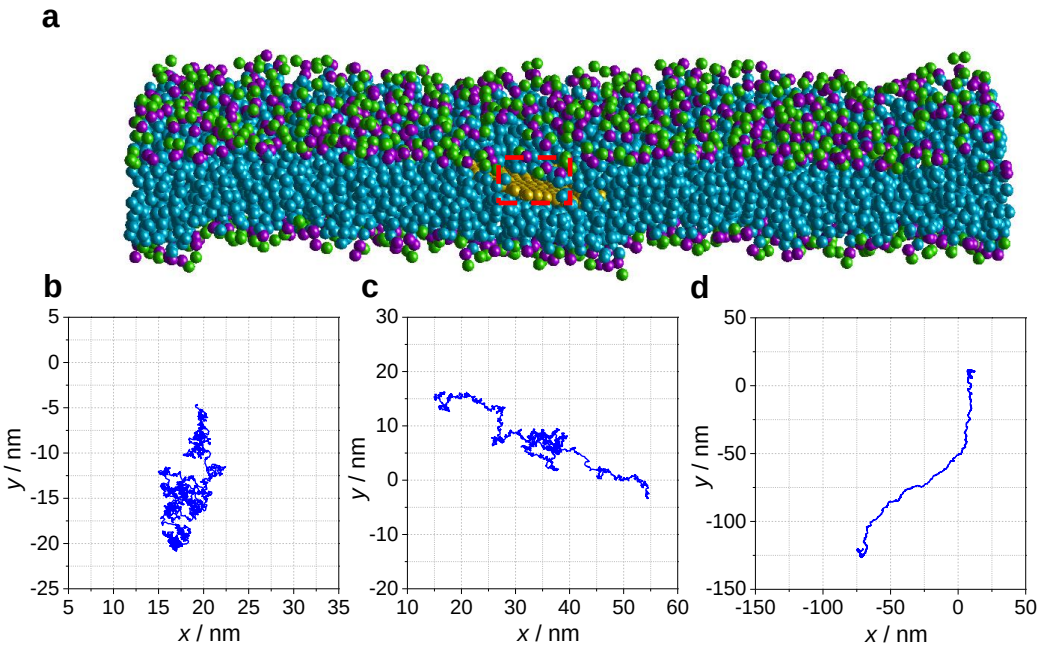

Fig. S12. Transition of diffusion patterns of the sandwiched GO from Brownian to Lévy and even directional dynamics with a membrane size of $40\times40\,r_c^2$**. a**, Typical pore states in cross-sectional view. The red circles display the pore induced by the sandwiched GO. **b-d**, Representative trajectories tracked for 1×10^4 τ, when the interaction parameter between GO and lipid tail, χ_{GT}, is: (B) 1.43; (C) 10.05; and (D) 14.3.

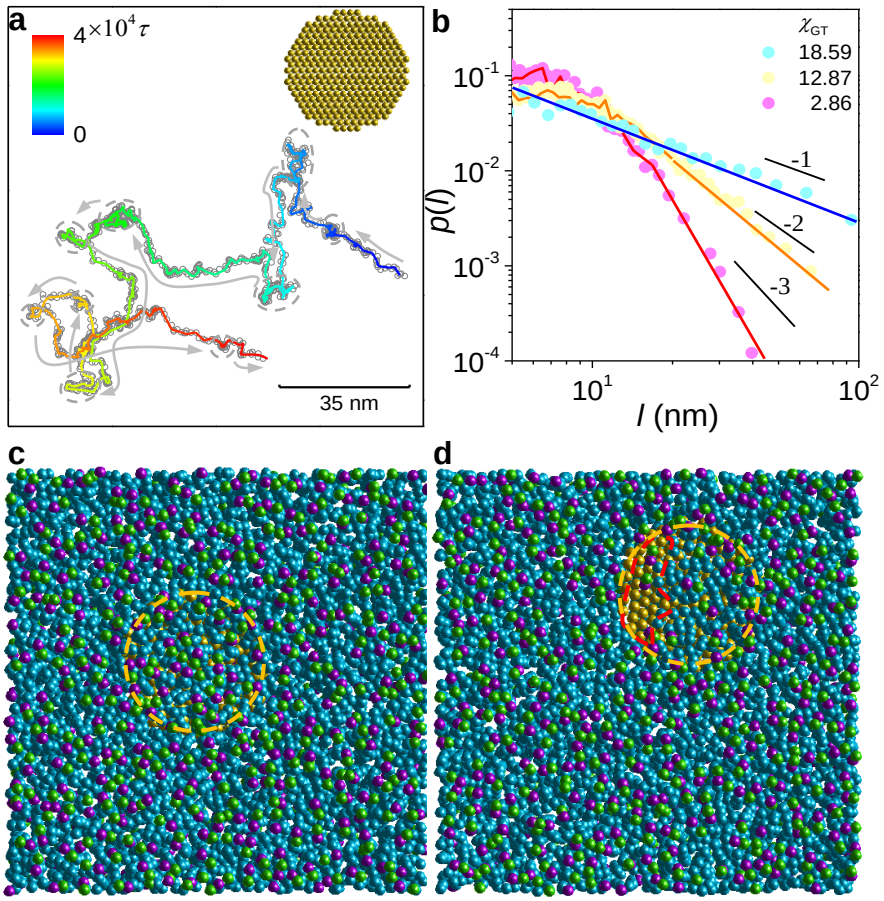

Fig. S13. Diffusive dynamics and membrane-pore states of a circular GO. a, Representative trajectories tracked for $4\times10^4\tau$, when the interaction parameter between GO and lipid tail, χ_{GT} =12.87. Colors denote the time lapse of the trajectory. Arrows and dashed circles indicate respectively alternating persistent segments and jiggling periods which are quantitatively identified by wavelet analysis. Circular GO is also modeled by arranging the beads on a single layer of fcc (face-centered cubic) lattice into a desired radius of 4.9nm (yellow) shown in the inset. **b**, The probability distribution of step length, *l*, on log-log scales, showing exponential statistics at χ_{GT} =2.86 but power-law statistics with slope -2 at χ_{GT} =10.01 and -1 at χ_{GT} =18.59 from maximum likelihood estimation of the power-law tails. **c** and **d**, Representative snapshots of membrane-pore states at χ_{GT} =2.86 (**c**) and 10.01 (**d**). The red circles display the pore induced by the sandwiched GO. The color scheme of beads is the same as those of fig. S6. Solvent beads are not shown for clarity.

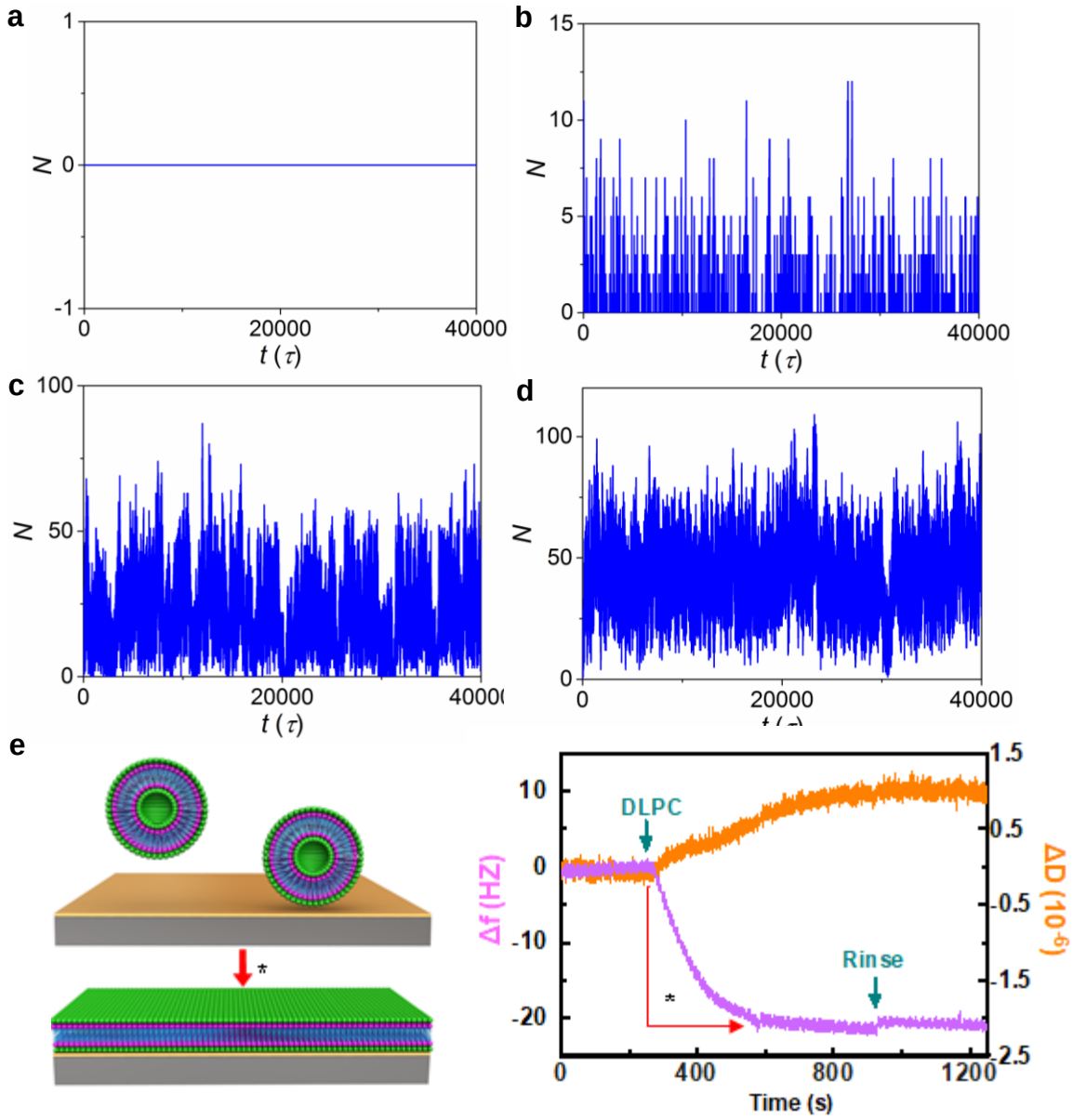

Fig. S14. Simulation results demonstrate various membrane-pore states and the mechanism of pore formation. a-d, The number of GO beads contacting solvent, *N*, is plotted as a function of time, *t*, at various χ_{GT}: **a**, 1.43; **b**, 7.15; **c**, 10.01; and **d**, 14.3. *N* indicates the size of the pore in a leaflet of the membrane. **e**, QCM data showing the formation of DLPC bilayer (indicated by the star *) through support-induced spreading of lipid vesicles on the chip.

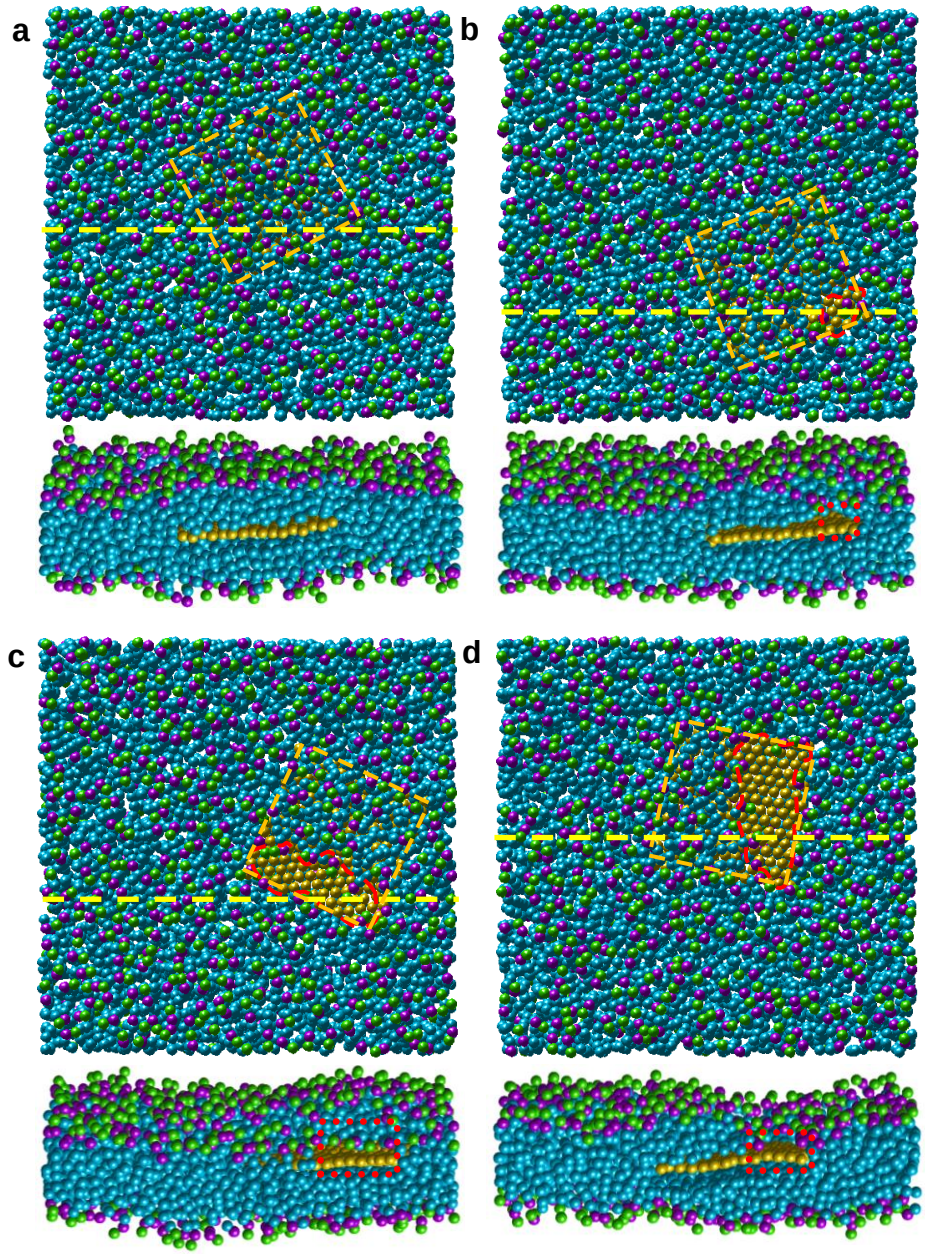

Fig. S15. Representative snapshots from simulations feature the sandwiched GO–induced pores in the single leaflet of cell membranes. Typical pore states in top view (top) and cross-sectional view along the dashed lines (bottom) are illustrated at various GO-lipid tail interactions χ_{GT} : **a**, 1.43; **b**, 7.15; **c**, 10.01; and **d**, 14.3. The dashed squares mark the contour of GO; the red circles display the pore induced by the sandwiched GO. The color scheme of beads is the same as that of fig. S6. Solvent beads are not shown for clarity.

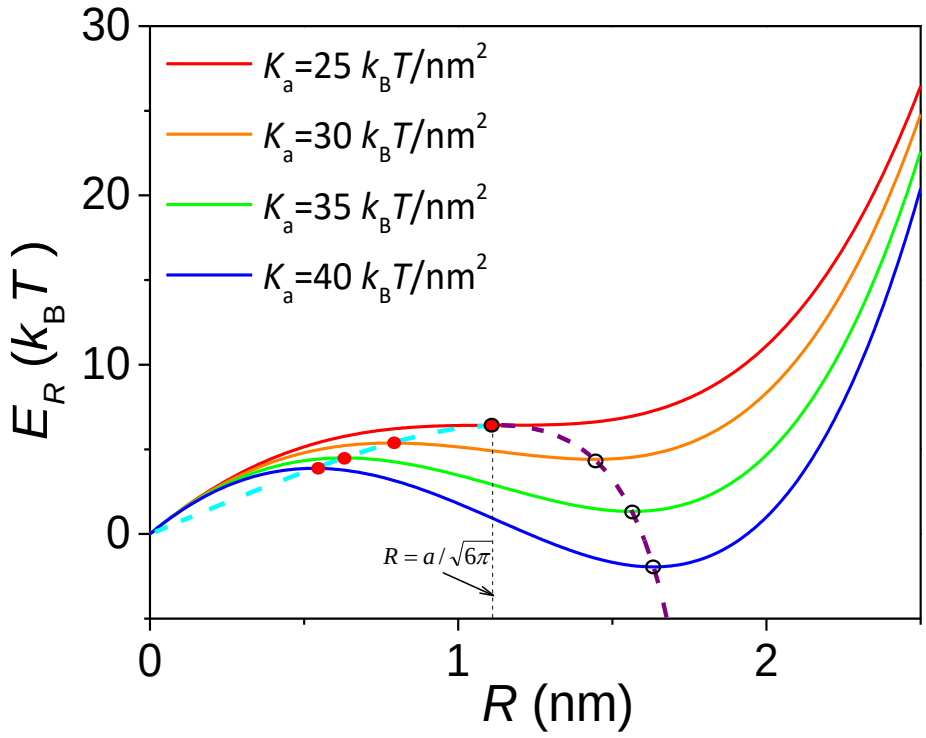

Fig. S16. The energy of the sandwiched GO–induced pore as a function of the radius of the pore *R* at $K_a \geq K_{a0}$ $(K_{a0} \approx 25\, k_B T / \mathrm{nm}^2)$**.** The plots are obtained by the analytical model. When K_a=K_{a0} (red curve), there are repeated roots $R_{01} = R_{02} = a/\sqrt{6\pi}$ (vertical dashed line) for $\partial_R E_R = 0$, where $\partial_R^2 E_R = 0$ also. When K_a>K_{a0}, with the increase of K_a, the minimum value R_{01} increases, while the maximum value R_{02} decrease, as indicated by the dashed purple and cyan curves, respectively. The solid and hollow circles at each plot mark the local maximum and the local minimum of E_R, namely, R_{02} and R_{01}, for the corresponding K_a. These both types of points meet at the transition point, *i.e.*, $R_{01} = R_{02} = a/\sqrt{6\pi}$.

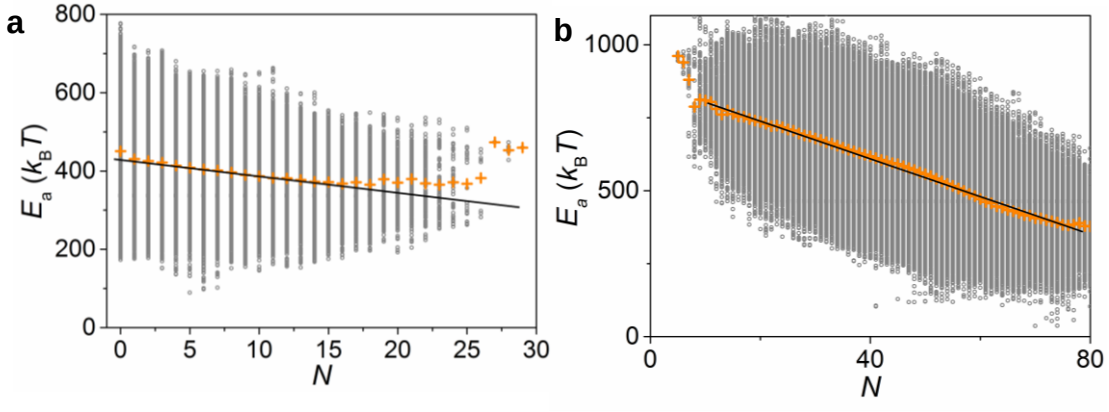

Fig. S17. Correlation between the analytical model and simulation results. Plot of lipid tail-GO interaction energy, E_a, versus the number of GO beads contacting solvent N, where χ_{GT} is: **a**, 7.15 and **b**, 14.3. Averaged from 5 million time steps (raw data obtained from simulation results and shown as gray circles), the yellow crosses have the linear fitting indicated in each figure.

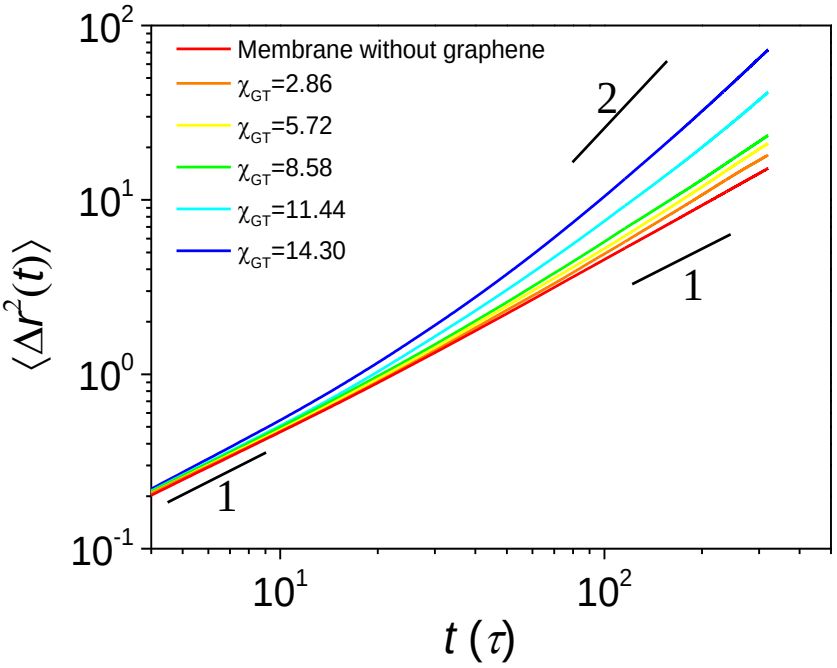

Fig. S18. Diffusive dynamics of lipids varies from Fickian to superdiffusive. Time Averaged mean square displacement $\langle \Delta r^2(t) \rangle$ of lipids is plotted as a function of lag time on log-log scales with different GO-lipid tail interactions.

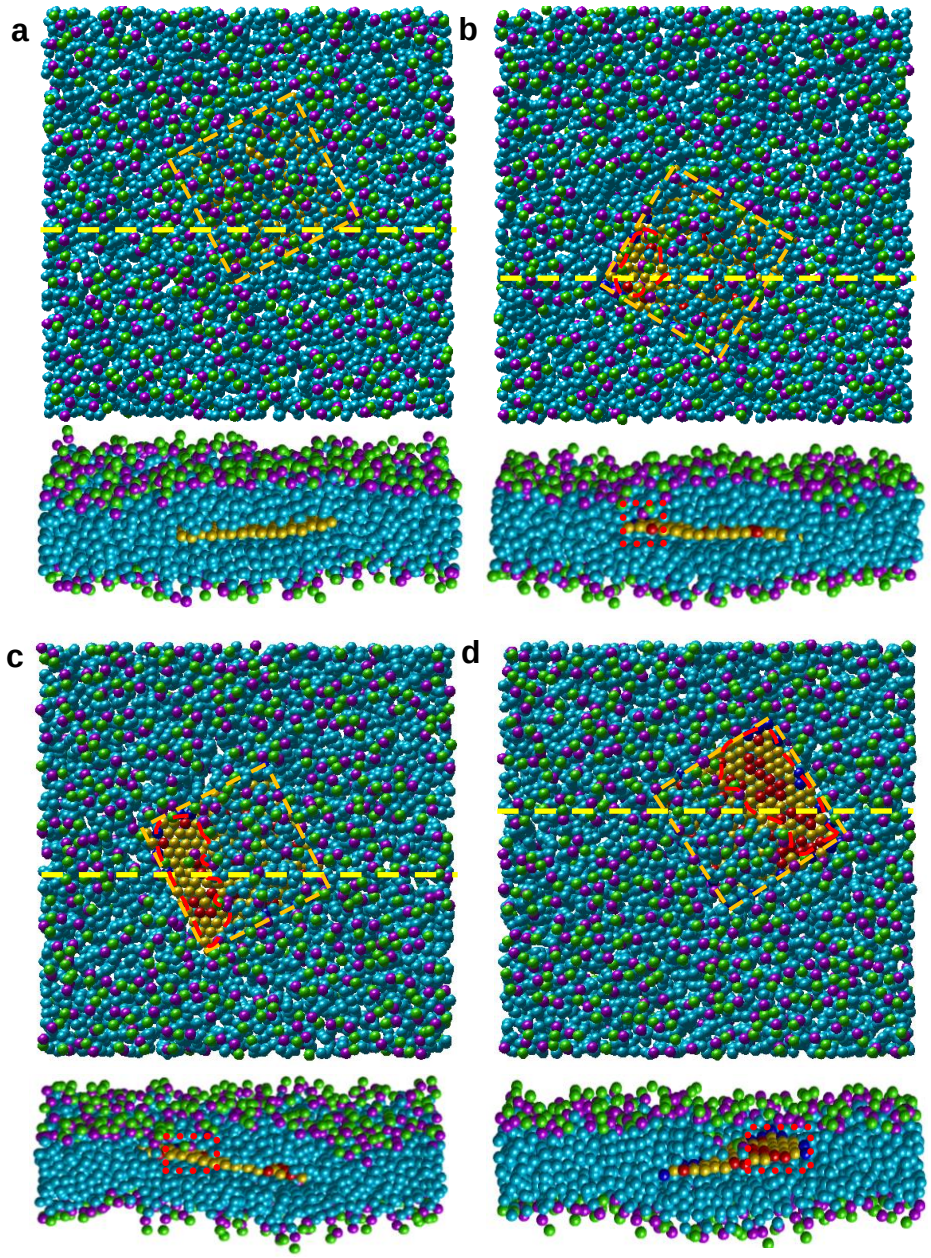

Fig. S19. Sandwiched GO–induced pores in the single leaflet of the cell membrane for the GO model representing outcomes from standard oxidization processes. Typical pore states in top view (top) and cross-sectional view along the dashed lines (bottom) are illustrated at various oxidation degrees ρ_O: **a**, 0; **b**, 0.1; **c**, 0.2; and **d**, 0.3. The dashed squares mark the contour of GO; the red circles display the pore induced by the sandwiched GO. The color scheme of beads is the same as that of fig. S8. Solvent beads are not shown for clarity.

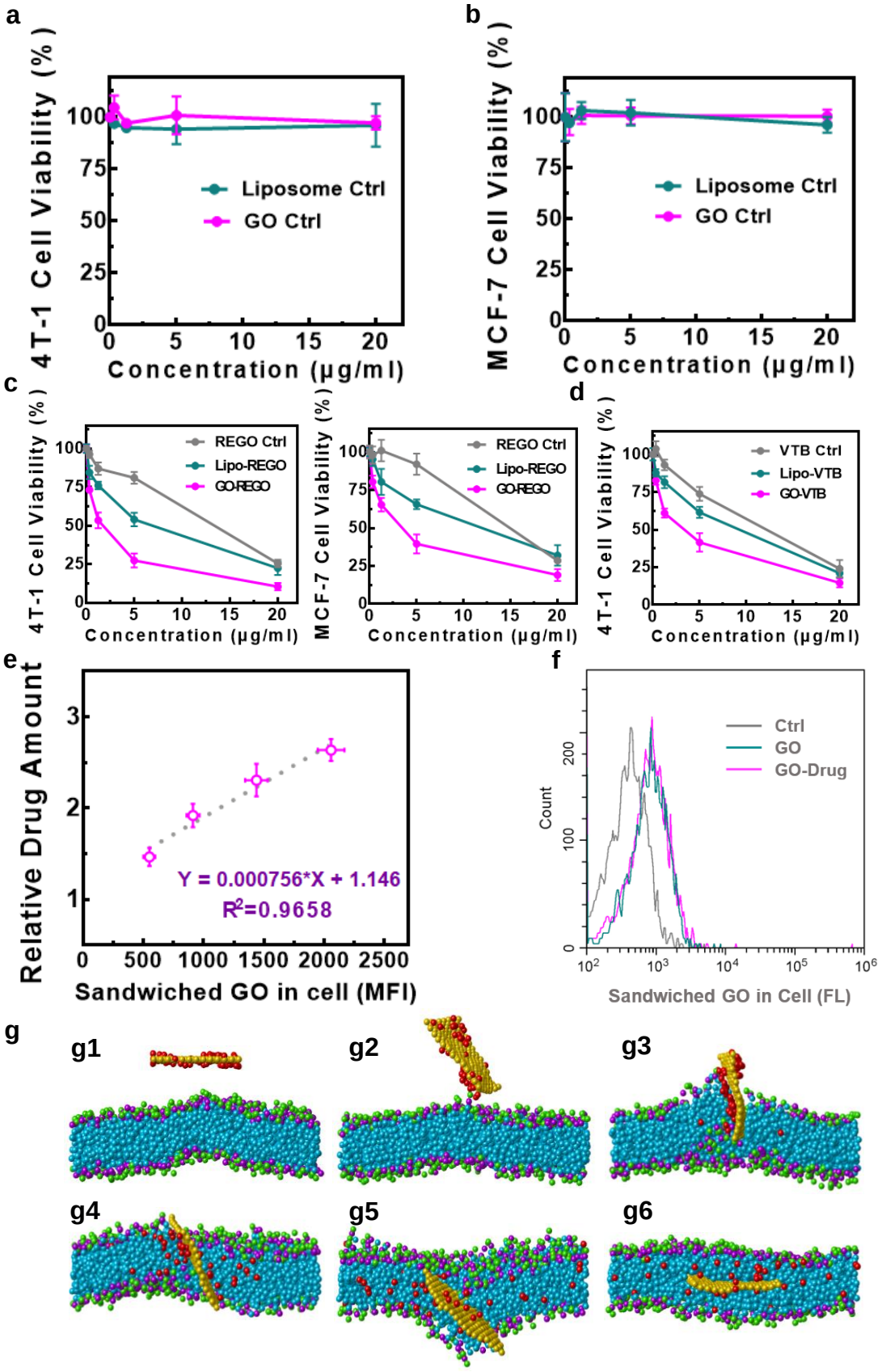
a
4T-1 Cell Viability (%)
Liposome Ctrl
GO Ctrl
Concentration (μg/ml)
b
MCF-7 Cell Viability (%)
Liposome Ctrl
GO Ctrl
Concentration (μg/ml)
c
4T-1 Cell Viability (%)
REGO Ctrl
Lipo-REGO
GO-REGO
Concentration (μg/ml)
MCF-7 Cell Viability (%)
REGO Ctrl
Lipo-REGO
GO-REGO
Concentration (μg/ml)
d
4T-1 Cell Viability (%)
VTB Ctrl
Lipo-VTB
GO-VTB
Concentration (μg/ml)
e
Relative Drug Amount
Y = 0.000756*X + 1.146
R2=0.9658
Sandwiched GO in cell (MFI)
f
Ctrl
GO
GO-Drug
Count
Sandwiched GO in Cell (FL)
g
g1
g2
g3
g4
g5
g6

Fig. S20. The efficacy of the GO-sandwiched structure on drug delivery. CCK8 data of cells after exposure with GO (a) and Liposomes (b) showing that the cell viability is almost unchanged in the absence of drug (at present dosage). **c-d**, The viability of cells after exposure to different membrane receptor inhibitors REGO (c) and VTB (d) with the assistant of GO or liposome in different cancer cells. In comparison with liposome group or drug control, GO group shows improved cell cytotoxicity, which again demonstrated the superior efficacy of membrane-specific delivery. **e**, The correlation between the sandwiched structure in cell and the relative intramembrane drug amount. The mean fluorescence intensity (MFI) of cells is assayed by using flow cytometry, where the fluorescence is sourced from the sandwiched GO at an excitation of NIR laser. The drug amount in different treated cells is detected by using LC-MS, which are normalized to the drug control group (GO-free). Results show that the sandwich structures in the cell membrane is indeed in correlation to intracellular drug amounts, which further confirm the potential of sandwiched structure for biomedical delivery. **f**, Flow cytometry histograms of the sandwiched structure signal for the pristine GO and drug loaded GO. The GO's entry into the membrane is not impeded by the absorbed drugs as indicated by the overlay histograms for GO and GO-Drug (VTB). **g**, Simulation of GO with drug molecules absorbed on the surface with lipid membrane towards the GO-sandwiched structure. The times of the slices are: **g1**, 0τ; **g2**, 360τ; **g3**, 440τ; **g4**, 520τ; **g5**, 632τ; and **g6**, 720τ. The color scheme of beads is the same as that of Fig. 6D. Solvent beads are not shown. Only the *x*-*z* cross section view of the lipid membrane around the GO is shown in each snapshot for clarity.

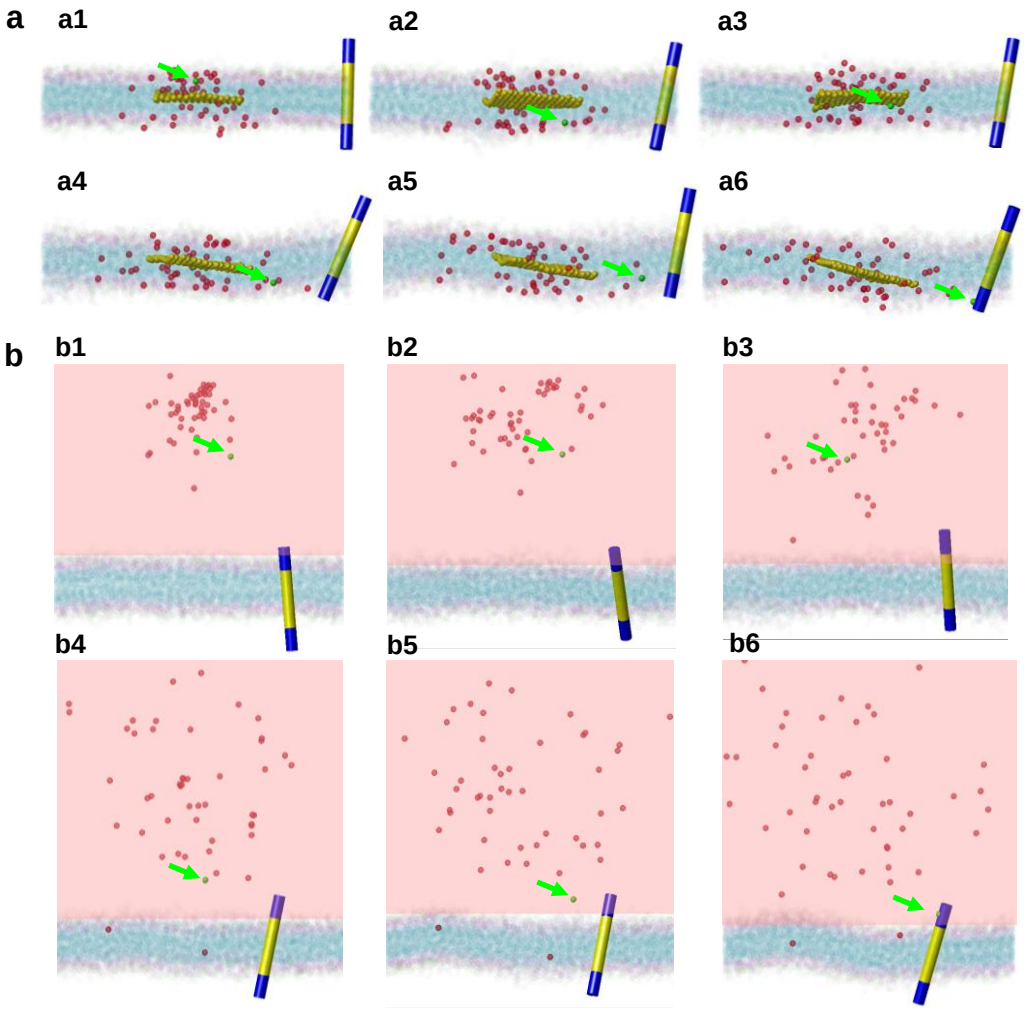

Fig. S21. Diffusive dynamics of a representative drug bead captured by the transmembrane receptor. a, Successive stages showing the detailed diffusion pathway of the drug beads from the sandwiched GO, where the number of drug beads are 50. The times of the simulation snapshots are: **a1**, 4 τ; **a2**, 12 τ; **a3**, 16 τ; **a4**, 40 τ; **a5**, 72 τ; and **a6**, 120 τ. **b**, Successive stages showing the detailed diffusion pathway of the drug beads from the center of the intracellular region, where the number of drug beads are 50. The times of the simulation snapshots are: **b1**, 8 τ; **b2**, 92 τ; **b3**, 192 τ; **b4**, 264 τ; **b5**, 296 τ; and **b6**, 336 τ. The color scheme of beads is the same as that of Fig. **6D**, except that the representative drug bead, which will be captured by the transmembrane receptor, is marked in green and denoted by the green arrow. All the lipid beads are half-transparent for clarity.

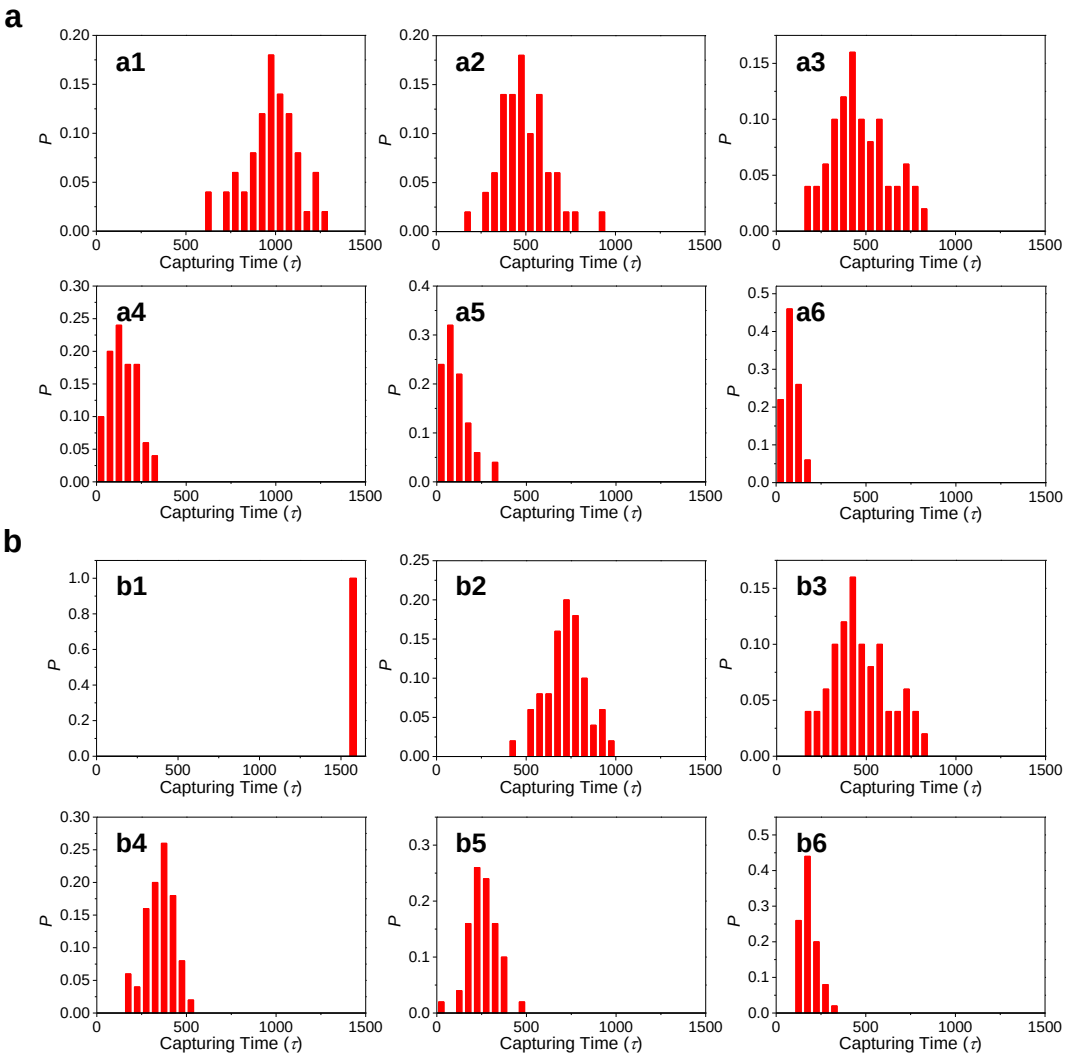

Fig. S22. Probability distribution of the capturing time for the drug beads released from the sandwiched GO and the center of the intracellular region. **a**, From a sandwiched GO at various number of drug beads: **a1**, 10; **a2**, 20; **a3**, 30; **a4**, 40; **a5**, 50; and **a6**, 100. **b**, From the center of the intercellular region at various number of drug beads: **b1**, 10; **b2**, 20; **b3**, 30; **b4**, 40; **b5**, 50; and **b6**, 100.